CORA Cork Open Research Archive
Cartlann Taighde Oscailte Chorcaí

Title	Continental configuration controls ocean oxygenation during the Phanerozoic
Authors	Pohl, Alexandre;Ridgwell, Andy;Stockey, Richard G.;Thomazo, Christophe;Keane, Andrew;Vennin, Emmanuelle;Scotese, Christopher R.
Publication date	2022-08-17
Original Citation	Pohl, A., Ridgwell, A., Stockey, R. G., Thomazo, C., Keane, A., Vennin, E. and Scotese, C. R. (2022) 'Continental configuration controls ocean oxygenation during the Phanerozoic', Nature, 608(7923), pp.523-527. https://doi.org/10.1038/s41586-022-05018-z
Type of publication	Article (peer-reviewed);journal-article
Link to publisher's version	10.1038/s41586-022-05018-z
Rights	© 2022, the Authors, under exclusive licence to Springer Nature Limited. This is a post-peer-review, pre-copyedit version of an article published in Nature. The final authenticated version is available online at: https://doi.org/10.1038/s41586-022-05018-z
Download date	2026-11-03 15:59:02
Item downloaded from	https://hdl.handle.net/10468/17393

UCC
University College Cork, Ireland
Coláiste na hOllscoile Corcaigh

Continental configuration controls ocean oxygenation during the Phanerozoic

Alexandre POHL[1,2*], Andy RIDGWELL[1*], Richard G. STOCKEY[3], Christophe THOMAZO[2,4], Andrew KEANE[5], Emmanuelle VENNIN[2], Christopher R. SCOTESE[6]

[1]Department of Earth and Planetary Sciences, University of California, Riverside, CA, USA

[2]Biogéosciences, UMR 6282, UBFC/CNRS, Université Bourgogne Franche-Comté, 6 boulevard Gabriel, F-21000 Dijon, France

[3]Department of Geological Sciences, Stanford University, Stanford, CA 94305, USA

[4]Institut Universitaire de France, Paris, France

[5]School of Mathematical Sciences and Environmental Research Institute, University College Cork, Cork, Ireland

[6]Department of Earth and Planetary Sciences, Northwestern University, Evanston, Illinois 60208, USA

[*]These authors contributed equally to this work

ABSTRACT

The early evolutionary and much of the extinction history of marine animals, is thought to be driven by changes in dissolved oxygen concentrations ([O_2]) in the ocean[1–3]. In turn, [O_2] is widely assumed to be dominated by the geological history of atmospheric oxygen (pO_2)[4,5]. Here, in contrast, we show via a series of Earth system model experiments how continental rearrangement during the Phanerozoic drives profound variations in ocean oxygenation and induces a fundamental decoupling in time between upper-ocean and benthic [O_2]. We further identify the presence of state transitions in the global ocean circulation, which lead to extensive deep-ocean anoxia developing in the early Phanerozoic even under modern pO_2. The occurrence of stable kyr-scale oscillations in ocean oxygenation that we find also provides a causal mechanism that might explain elevated rates of metazoan radiation and extinction during the early Paleozoic[6]. The absence, in our modelling, of any simple correlation between global climate and ocean ventilation, and the occurrence of profound variations in ocean oxygenation independent of atmospheric pO_2, presents a challenge to the interpretation of marine redox proxies, but also points to a hitherto unrecognized role for continental configuration in the evolution of the biosphere.

MAIN TEXT

The availability of dissolved oxygen in the ocean exerts a critical control on habitability for marine animals[1,7] and is thought to have dramatically impacted their evolution from the late Neoproterozoic and through the Phanerozoic Eon (541-0 Ma)[1–3]. Indeed, the emergence of the first unambiguous metazoans during the Ediacaran period (635–541 Ma) may have been triggered by the occurrence of ambient [O_2] sufficient to support the metabolism of a large body size[1]. Further increases in ocean oxygenation may have contributed to the Great

Ordovician Biodiversification Event[8] as well as the rise of large predatory fish in the Devonian[9]. Conversely, episodic deoxygenation is considered the primary kill mechanism during many of the major Phanerozoic mass extinction events, including the Late Ordovician[10], Late Devonian[11] and end Permian[7].

The past few decades have seen the development and application of a variety of geochemical redox proxies such as $\delta^{238}U$[12], $\delta^{98}Mo$[9], I/Ca[13] and iron speciation[14], which have provided us with unprecedented insights into the Phanerozoic history of ocean oxygenation[5,13]. In parallel, numerical models have been instrumental in helping interpret the proxy trends and test hypotheses for the underlying driving mechanisms[4,15]. Principal amongst the ideas that have arisen is that changes in atmospheric pO_2 can be inferred from the ocean[4,5,15]. However, for computational reasons, this link between ocean $[O_2]$ and atmospheric pO_2 has invariably been made without considering how ocean circulation may have changed through time[4,5,15]. While the importance of continental configuration for ocean circulation and surface climate has started to be studied systematically[16–18], spatial patterns of ocean geochemistry and redox have only been considered in a limited number of continental configurations (e.g. refs[7,19]) and often analyzed in temporal isolation. Here we explicitly address this gap, employing an Earth System Model of intermediate complexity to quantify how continental configuration can modulate the distribution of $[O_2]$ in the ocean, thereby leading us to a radically different conclusion regarding the inferences that can be drawn from marine redox proxy records.

We base our analysis on a series of past ocean circulation scenarios generated using cGENIE[20], an Earth System Model of intermediate complexity designed to simulate the large-scale biogeochemical cycles and patterns in the ocean, and one that has previously been shown to be capable of simulating regional-scale distributions of $[O_2]$ in the present-day ocean[20] as well as in the geological past[19,21] (see Methods, Extended Data Fig. 1). In these experiments, we consider both the potential role of changing ecological structure in the ocean

(using the size-structured plankton model of ref[22]) as well as the influence of temperature on metabolic rates (following ref[23]) in creating 3D realizations of the potential distribution of [O_2] in the ocean. Based on the continental reconstructions of Scotese and Wright[24], we conducted one simulation every 20 Myrs through the Phanerozoic, for a total of 28 simulated time slices. In order to help isolate the impact of continental configuration from other changes occurring through the Phanerozoic, only the continental configuration[24] (plus physical atmospheric boundary conditions – see Methods) was varied from one time slice to the other. Solar luminosity (1368 W m^{-2}), atmospheric oxygen concentration (20.95 %), and ocean nutrient inventory (2.1 μmol kg^{-1} PO_4) were kept identical in every model run, and in a first series of simulations (#1), we also kept atmospheric pCO_2 fixed (at 2240 ppm, see Methods). We hence are not aiming to reconstruct the Phanerozoic evolution of climate here (see e.g. refs[16,18]), nor necessarily provide a reconstruction of past [O_2] in the ocean or even recover modern distributions with high fidelity, but rather, expose the specific impact of changes in continental configuration on gross ocean oxygenation.

Despite assuming both invariant solar constant and pCO_2, substantive variability in climate through the Phanerozoic occurs in the model (Fig. 1b). This is an expected result of sea-level driven changes in the proportion of absorptive ocean surface vs. more reflective land surface[17,25] as well as of continental latitudinal distribution, and in a principal component analysis conducted across all 28 time slices we find a strong positive correlation between global mean sea-surface temperature (SST) and global ocean surface area (Fig. 1e; $R^2 = 0.585$). Given our assumption of invariant pO_2 (deliberately chosen to expose the role of the continental configuration), we find a relatively straightforward and expected inverse relationship between mean ocean surface [O_2] and SST (Fig. 1b, e) – driven primarily via changes in oxygen solubility and modulated by the latitudinal distribution of ocean surface area. Global mean subsurface (ca. 90–190 m depth in the model) [O_2] exhibits a more

97 exaggerated temporal evolution (Fig. 1c). Respiration of organic matter exported from the
98 ocean surface now strongly amplifies subsurface oxygen variability (Fig. 1c, e) and
99 introduces new features unconnected to SST changes, such as the ~35 μmol kg^{-1} decrease
100 from 460 to 400 Ma. This is our first hint of the importance of changing continental
101 distribution and hence large-scale pattern of ocean circulation, which in the case of
102 subsurface [O_2] is via changes in the resupply of nutrients to the surface. Even without
103 attempting to simulate a realistic sequence of Phanerozoic climate states (and hence changing
104 ocean surface oxygen solubility), our modelling provides hints as to the timing of Oceanic
105 Anoxic Events (OAEs) during the Phanerozoic (Fig. 2, Extended Data Fig. 2). For instance,
106 seafloor ocean deoxygenation develops in the paleo-Tethys during the Permian-Triassic
107 transition (ca. 260 Ma)[26] and in the central Atlantic during the Early Cretaceous (ca. 120
108 Ma)[27] and Late Cretaceous (ca. 100 Ma)[28]. That the Late Devonian OAE (380 Ma)[29] and
109 Toarcian OAE (ca. 180 Ma)[30] are not captured by our simulations may be a result of the
110 coarse model grid (for the Tethys Ocean during the Toarcian OAE in particular[30]; Fig. 2,
111 Extended Data Fig. 2). This could also be interpreted as reflecting the need for a strong
112 perturbation (warming and nutrient-driven increase in primary productivity) at that time to
113 trigger an OAE, since the continental configuration itself is not particularly prone to ocean
114 deoxygenation in our model simulations.
115 Our unexpected discovery from the numerical modelling is how variable global deep-
116 ocean [O_2] (calculated as the mean of all benthic grid points in the model below 1000 m
117 depth) is (Fig. 1d); ranging from 30 μmol kg^{-1} (and near fully anoxic) to 178 μmol kg^{-1} (a
118 little higher than modern). The early Paleozoic (541 to 460 Ma) in particular stands out, and
119 is characterized by anomalously poor deep seafloor oxygenation (generally < 45 μmol kg^{-1})
120 in the model, with an abrupt rise to 171 μmol kg^{-1} at 440 Ma and thereafter mostly remaining
121 above 100 μmol kg^{-1} (Fig. 1d). The step change in benthic oxygenation simulated between

460 Ma and 440 Ma is similarly observed using an alternative set of continental reconstructions[31] (Extended Data Fig. 4). Simulated water age (the mean time since a water parcel was last exposed to the atmosphere) anti-correlates with mean global and benthic [O_2] (Fig. 1d, e), while SST and global water age do not correlate (Fig. 1e; $R^2 = 0.001$), pointing to the dominance of a paleogeographical control on deep-ocean oxygenation.

To further simplify the attribution of causes of benthic [O_2] variability through the Phanerozoic and eliminate global climate change and resulting solubility-driven upper-ocean [O_2] variations as explanatory factors, we carried out a second series of model experiments (#2) in which we kept mean global SST and surface oxygenation largely invariant (Fig. 3). Climate detrending was achieved by varying pCO_2 in the model. Variance in mean benthic [O_2] (Fig. 3d) is now if anything, even greater than in #1 (Fig. 1d) and the general trend of a poorly oxygenated early Paleozoic deep ocean still stands. These results confirm that benthic anoxia in the early Paleozoic ocean results from changes in the deep-ocean circulation in the model, rather than temperature-driven variations in upper-ocean [O_2]. Sensitivity tests demonstrate that global mean temporal trends and spatial oxygenation patterns are largely independent of whether a temperature-dependent (Fig. 1) or fixed remineralization profile (Extended Data Fig. 5) is assumed. Similarly, patterns of benthic [O_2] are only weakly impacted by uncertainties in the position of mid-ocean ridges (Extended Data Figs. 6, 7).

The role of continental configuration in creating conditions of extreme deep-ocean deoxygenation and weakened ventilation (old water mass ages) during the early Paleozoic (prior to 440 Ma in series #1 (Fig. 1d), and prior to 420 Ma in series #2 (Fig. 3d)), arises from the existence of state transitions in the large-scale circulation of the ocean in the model. Using series #1 as an example, the oldest time slices (540 – 500 Ma) are characterized by a poorly ventilated seafloor with deep waters forming over the South Pole (Figs. 1d and 2, Extended Data Fig. 8a). At 480 and 460 Ma, the ocean circulation oscillates between the

147 previous poorly-ventilated state and a better-ventilated state, the latter state subsequently
148 becoming stabilized at 440 Ma by further tectonic rearrangement (Figs. 1d and 2, Extended
149 Data Fig. 8a). Of course, the differences in the two simulation series illustrate that the climate
150 state also influences the ocean circulation regimes (contrast Figs. 1 and 3; see also Extended
151 Data Figs. 8 and 9). Several lines of evidence suggest that these state transitions are a robust
152 characteristic of the early Paleozoic, at least in the cGENIE model. Indeed, additional
153 simulations conducted using idealized land-sea masks reveal that these state transitions may
154 be a characteristic feature of continental configurations with one pole free of land (Extended
155 Data Fig. 10; Methods), such as the one of the early Paleozoic (Fig. 2), and a similar
156 reorganization of the global ocean circulation has previously been shown to best explain the
157 expansion of seafloor anoxia during Late Ordovician glaciation (Extended Data Fig. 10 and
158 ref.[21]).

159 The occurrence of climate-driven state transitions in ocean circulation and oxygenation
160 is well established in the context of changes in Atlantic and Pacific basin meridional
161 overturning since the last glacial maximum (21 ka)[32,33]. In contrast, the potential for ocean
162 state transitions in deeper time has received much less attention but is no less important (e.g.
163 ref.[21]). We also have good reason to conclude that the occurrence of oscillatory ocean
164 circulation modes is not an artifact of the particular model used here and may occur as a
165 transitional regime between different stable steady-states (Extended Data Fig. 10). For
166 instance, oscillations have previously been identified in both (ocean-only) 3D ocean
167 circulation models[34,35] and 3D ocean circulation models coupled to simplified representations
168 of atmospheric dynamics (Earth System Models of intermediate complexity)[36,37]. Non-steady
169 solutions in volume-integrated ocean temperature are also hinted at in a number of recent
170 fully coupled GCM simulations under specific continental configurations and climate
171 states[16]. Further work conducted using higher-resolution Earth system models, e.g. of the

Coupled Model Intercomparison Project phase 6 generation, will be important to distinguish robust from model-dependent modes of ocean circulation, although identifying the boundary conditions giving rise to oscillatory modes will be computationally challenging.

Our finding of a fundamental decoupling of subsurface and benthic [O_2] during the Phanerozoic (Fig. 1e; $R^2 = 0.001$) implies that no simple relationship exists during the Phanerozoic amongst the concentrations of oxygen in the atmosphere, the subsurface ocean, and at the seafloor. Furthermore, the highly non-linear and chaotic nature of the system means that even very minor changes in continental configuration (e.g. contrast 460 vs. 440 Ma, Figure 2) can induce dramatic re-organizations of large-scale circulation and hence ocean oxygenation, and similarly, confusticate any predictable relationship between changes in atmospheric pCO_2 (and climate) and ocean oxygenation. This has implications not only for how we interpret deep-ocean redox proxy records and specifically proxies for the global areal extent of seafloor anoxia[5] (e.g., $\delta^{238}U$[12], $\delta^{98}Mo$[9]), but also how we understand the underlying controls on ocean anoxia and infer changes in atmospheric composition. For instance, Stolper and Keller[38] analyzed the ratio of Fe^{3+} to total Fe ($Fe^{3+}/\Sigma Fe$) in hydrothermally altered basalts formed in ocean basins to quantitatively reconstruct deep-ocean [O_2] over the last 3500 Myrs. Their results suggest that the deep ocean became oxygenated only in the Phanerozoic and probably not until the late Paleozoic (<420 Myr). Our simulations support the vision of a poorly oxygenated early Paleozoic ocean[4,5,38] (until ca. 440 Ma in the model, see Figs. 1d, 3d). However, while $Fe^{3+}/\Sigma Fe$ data is interpreted as reflecting a rise in atmospheric oxygen concentrations[38], our Earth System simulations in contrast suggest that deep-ocean oxygenation around 440–420 Ma could have been a consequence of continental rearrangement and concomitant changes in ocean circulation and ventilation. The implication is that early Phanerozoic atmospheric pO_2 need not have been appreciably lower than modern, which aligns with the measurements of atmospheric oxygen trapped in fluid-gas

inclusions of halite[39]. Furthermore, the step changes in early Paleozoic seafloor oxygenation are indicative of bistability between deep-ocean circulation states; that is, for certain continental configurations multiple advection and convection patterns will co-exist (what is observed depends on the initial conditions of the simulation). Switches between such states could provide an explanation to the swings[5] in early Paleozoic global anoxia extent documented on grounds of $\delta^{238}U$[40–42] and $\delta^{98}Mo$[41,43]. Uncertainties in both the model and geological data preclude us from determining if our simulated scenario may have actually taken place in the geological past, and we recognize that continental rearrangement is also not exclusive of secular variation in other drivers of ocean anoxia, such as atmospheric oxygen, ocean nutrient inventory, and global warming[13,19,21,26]. That said, and despite our idealized boundary conditions and invariant atmospheric chemistry, there are shared temporal trends (albeit with different timings and interval durations) with recent I/Ca-based oxygen proxy compilations[13], namely: low oxygenation in the early and late Paleozoic with a high during the Devonian, and peak values occurring prior to late Cenozoic cooling.

Finally, our results have implications for the evolution of marine animal ecosystems through the Phanerozoic. If kyr-scale oscillations in ocean oxygenation were a characteristic feature of early Paleozoic oceans, as supported by the high-resolution Mo record of ref.[44] and our modelling (Extended Data Fig. 8), this would lend support to arguments linking the progressive (here: paleogeographical) stabilization of a steady-state Earth system to decreasing extinction rates through the Phanerozoic[6,45].

MAIN TEXT REFERENCES

1. Payne, J. L. *et al.* Two-phase increase in the maximum size of life over 3.5 billion years reflects biological innovation and environmental opportunity. *Proc. Natl. Acad. Sci. U. S. A.* **106**, 24–27 (2009).

2. Cole, D. B. *et al.* On the co-evolution of surface oxygen levels and animals. *Geobiology* **18**, 260–281 (2020).

3. Sperling, E. A., Knoll, A. H. & Girguis, P. R. The Ecological Physiology of Earth's Second Oxygen Revolution. *Annu. Rev. Ecol. Evol. Syst.* **46**, 215–235 (2015).

4. Krause, A. J. *et al.* Stepwise oxygenation of the Paleozoic atmosphere. *Nat. Commun.* **9**, 4081 (2018).

5. Tostevin, R. & Mills, B. J. Reconciling proxy records and models of Earth's oxygenation during the Neoproterozoic and Palaeozoic. *Interface Focus* **10**, 20190137 (2020).

6. Kocsis, Á. T., Reddin, C. J., Alroy, J. & Kiessling, W. The r package divDyn for quantifying diversity dynamics using fossil sampling data. *Methods Ecol. Evol.* **10**, 735–743 (2019).

7. Penn, J. L., Deutsch, C., Payne, J. L. & Sperling, E. A. Temperature-dependent hypoxia explains biogeography and severity of end-Permian marine mass extinction. *Science* **362**, eaat1327 (2018).

8. Edwards, C. T., Saltzman, M. R., Royer, D. L. & Fike, D. A. Oxygenation as a driver of the Great Ordovician Biodiversification Event. *Nat. Geosci.* **10**, 925–929 (2017).

9. Dahl, T. W., Hammarlund, E. U. & Anbar, A. D. Devonian rise in atmospheric oxygen correlated to the radiations of terrestrial plants and large predatory fish. *Proc. Natl. Acad. Sci.* **107**, 17911–17915 (2010).

10. Zou, C. *et al.* Ocean euxinia and climate change "double whammy" drove the Late Ordovician mass extinction. *Geology* **46**, 535–538 (2018).

11. Bond, D., Wignall, P. B. & Racki, G. Extent and duration of marine anoxia during the Frasnian-Famennian (Late Devonian) mass extinction in Poland, Germany, Austria and France. *Geol. Mag.* **141**, 173–193 (2004).

12. Lau, K. V. *et al.* Marine anoxia and delayed Earth system recovery after the end-Permian extinction. *Proc. Natl. Acad. Sci.* **113**, 2360–2365 (2016).
13. Lu, W. *et al.* Late inception of a resiliently oxygenated upper ocean. *Science* **5**, eaar5372 (2018).
14. Sperling, E. A. *et al.* A long-term record of early to mid-Paleozoic marine redox change. *Sci. Adv.* (2021) doi:10.1126/sciadv.abf4382.
15. Lenton, T. M. *et al.* Earliest land plants created modern levels of atmospheric oxygen. *Proc. Natl. Acad. Sci. U. S. A.* 201604787 (2016).
16. Valdes, P., Scotese, C. & Lunt, D. Deep Ocean Temperatures through Time. *Clim. Past* **17**, 1483–1506 (2021).
17. Farnsworth, A. *et al.* Climate Sensitivity on Geological Timescales Controlled by Nonlinear Feedbacks and Ocean Circulation. *Geophys. Res. Lett.* **6**, 19 (2019).
18. Scotese, C. R., Song, H., Mills, B. J. W. & van der Meer, D. G. Phanerozoic paleotemperatures: The earth's changing climate during the last 540 million years. *Earth-Science Rev.* 103503 (2021) doi:10.1016/j.earscirev.2021.103503.
19. Monteiro, F. M., Pancost, R. D., Ridgwell, A. & Donnadieu, Y. Nutrients as the dominant control on the spread of anoxia and euxinia across the Cenomanian-Turonian oceanic anoxic event (OAE2): Model-data comparison. *Paleoceanography* **27**, (2012).
20. Ridgwell, A. *et al.* Marine geochemical data assimilation in an efficient Earth system model of global biogeochemical cycling. *Biogeosciences* **4**, 87–104 (2007).
21. Pohl, A. *et al.* Vertical decoupling in Late Ordovician anoxia due to reorganization of ocean circulation. *Nat. Geosci.* **14**, (2021).
22. Ward, B. A. *et al.* EcoGEnIE 0.1: plankton ecology in the cGENIE Earth system model. *Geosci. Model Dev.* **11**, 4241–5267 (2018).
23. Crichton, K. A., Wilson, J. D., Ridgwell, A. & Pearson, P. N. Calibration of key

temperature-dependent ocean microbial processes in the cGENIE. muffin Earth system model. *Geophys. Model Dev. Discuss.* (2020).

24. Scotese, C. R. & Wright, N. PALEOMAP Paleodigital Elevation Models (PaleoDEMS) for the Phanerozoic (PALEOMAP Project, 2018). https://www.earthbyte.org/paleodem-resource- scotese-and-wright-2018/ (2018).

25. Pohl, A. *et al.* Quantifying the paleogeographic driver of Cretaceous carbonate platform development using paleoecological niche modeling. *Palaeogeogr. Palaeoclimatol. Palaeoecol.* **514**, 222–232 (2019).

26. Hülse, D. *et al.* End-Permian marine extinction due to temperature-driven nutrient recycling and euxinia. *Nat. Geosci.* **14**, (2021).

27. Baudin, F. & Riquier, L. The late hauterivian faraoni 'oceanic anoxic event': An update. *Bull. la Soc. Geol. Fr.* **185**, 359–377 (2014).

28. Laugié, M. *et al.* Exploring the impact of Cenomanian paleogeography and marine gateways on oceanic oxygen. *Paleoceanogr. Paleoclimatology* **36**, e2020PA004202 (2021).

29. De Vleeschouwer, D. *et al.* Timing and pacing of the Late Devonian mass extinction event regulated by eccentricity and obliquity. *Nat. Commun.* **8**, 2268 (2017).

30. Ruvalcaba Baroni, I. *et al.* Ocean Circulation in the Toarcian (Early Jurassic): A Key Control on Deoxygenation and Carbon Burial on the European Shelf. *Paleoceanogr. Paleoclimatology* **33**, 994–1012 (2018).

31. Torsvik, T. H. BugPlates : Linking Biogeography and Palaeogeography Software Installation. (2009).

32. Ferreira, D., Marshall, J., Ito, T. & McGee, D. Linking Glacial-Interglacial States to Multiple Equilibria of Climate. *Geophys. Res. Lett.* **45**, 9160–9170 (2018).

33. Jaccard, S. L. & Galbraith, E. D. Large climate-driven changes of oceanic oxygen

297 concentrations during the last deglaciation. *Nat. Geosci.* **5**, 151–156 (2012).
298 34. Weijer, W. & Dijkstra, H. A. Multiple oscillatory modes of the global ocean
299 circulation. *J. Phys. Oceanogr.* **33**, 2197–2213 (2003).
300 35. Sirkes, Z. & Tziperman, E. Identifying a damped oscillatory thermohaline mode in a
301 general circulation model using an adjoint model. *J. Phys. Oceanogr.* **31**, 2297–2306
302 (2001).
303 36. Meissner, K. J., Eby, M., Weaver, A. J. & Saenko, O. A. CO2 threshold for millennial-
304 scale oscillations in the climate system: Implications for global warming scenarios.
305 *Clim. Dyn.* **30**, 161–174 (2008).
306 37. Haarsma, R. J., Opsteegh, J. D., Selten, F. M. & Wang, X. Rapid transitions and ultra-
307 low frequency behaviour in a 40 kyr integration with a coupled climate model of
308 intermediate complexity. *Clim. Dyn.* **17**, 559–570 (2001).
309 38. Stolper, D. A. & Keller, C. B. A record of deep-ocean dissolved O2 from the oxidation
310 state of iron in submarine basalts. *Nature* **553**, 323–327 (2018).
311 39. Brand, U. *et al.* Atmospheric oxygen of the Paleozoic. *Earth-Science Rev.* **216**, (2021).
312 40. Dahl, T. W. *et al.* Reorganisation of earth's biogeochemical cycles briefly oxygenated
313 the oceans 520 myr ago. *Geochemical Perspect. Lett.* **10**, 210–220 (2019).
314 41. Wei, G. Y. *et al.* Global marine redox evolution from the late Neoproterozoic to the
315 early Paleozoic constrained by the integration of Mo and U isotope records. *Earth-*
316 *Science Rev.* **214**, 103506 (2021).
317 42. Wei, G. Y. *et al.* Marine redox fluctuation as a potential trigger for the Cambrian
318 explosion. *Geology* **46**, 587–590 (2018).
319 43. Kendall, B. *et al.* Uranium and molybdenum isotope evidence for an episode of
320 widespread ocean oxygenation during the late ediacaran period. *Geochim. Cosmochim.*
321 *Acta* **156**, 173–193 (2015).

44. Dahl, T. W. *et al.* Brief oxygenation events in locally anoxic oceans during the Cambrian solves the animal breathing paradox. *Sci. Rep.* **9**, 1–9 (2019).
45. Payne, J. L., Bachan, A., Heim, N. A., Hull, P. M. & Knope, M. L. The evolution of complex life and the stabilization of the Earth system: Complex life and the Earth system. *Interface Focus* **10**, (2020).
46. Cao, L. *et al.* The role of ocean transport in the uptake of anthropogenic CO2. *Biogeosciences* **6**, 375–390 (2009).

METHODS

Description of the model

cGENIE[20] – an 'Earth System Model of intermediate complexity' – is based around a 3-dimensional ocean circulation model which, for speed, is coupled to a 2D energy-moisture-balance atmospheric component. We configured the model on a 36×36 equal-area grid with 16 unevenly spaced vertical levels to a maximum 5500 m depth in the ocean. The cycling of carbon and associated tracers in the ocean is based on a single (phosphate) nutrient limitation of biological productivity accounting for plankton ecology based on Ward et al.[22] and Wilson et al.[47], but adopts the Arrhenius-type temperature-dependent scheme for the remineralization of organic matter exported to the ocean interior of Crichton et al.[23]. We further modify the ecological model of Ward et al.[22] to account for limitation of productivity under sea ice, re-scale the global mean annual C/P ratio of exported particulate organic matter to match that of the standard model (106)[46], and only diagnose the ocean surface mixed layer depth for calculating light attenuation rather than entrain this into the physical circulation. We include a sulphate (SO_4^{2-}) tracer as an electron acceptor in the model in addition to dissolved oxygen, such that when O_2 starts to approach zero, sulphate reduction occurs in association with the remineralization of organic matter. The hydrogen sulphide (H_2S) thereby created is transported via ocean circulation and oxidized in the presence of O_2 to re-form sulphate. Note that we do not include a nitrogen cycle (and hence nitrate reduction), nor methanogenesis in our model tracer configuration. See ref.[48] and ref.[49] for details of the overall ocean redox scheme.

Despite its low spatial resolution, cGENIE satisfactorily simulates first-order ocean [O_2] spatial patterns and values for the present-day ocean when configured with pre-industrial boundary conditions such as 278 ppm CO_2 (Extended Data Fig. 1 and ref.[20]), as well as in the geological past[19,21]. For instance, simulations for Oceanic Anoxic Event 2 conducted using

cGENIE (ref.[19], their Fig. 2f,g) compare well with simulations conducted using the more complex model IPSL-CM5A2 (ref.[28], their Fig. 10), in terms of both global extent of anoxia and response to gateway alteration.

Description of the numerical experiments

We adopted the (flat-bottomed) Phanerozoic continental reconstructions of Scotese and Wright[24], but substituted the deep-ocean bathymetry of Müller et al.[50] when available (140 Ma – 0 Ma) in order to account for mid-ocean ridges. In order to specifically quantify the impact of paleogeographical evolution, we kept solar luminosity (1368 W m^{-2}), atmospheric oxygen concentrations (20.95 %), and ocean nutrient inventory (2.1 μmol kg^{-1} PO_4), invariant. We employed a null eccentricity-minimum obliquity orbital configuration, which provides an equal mean annual insolation to both hemispheres with minimum seasonal contrasts. Atmospheric CO_2 concentration was kept fixed in series #1 (2240 ppm) but varied in series #2 in order to approximately 'correct' for the paleogeographical impacts on climate. These forcing combinations ensured that simulated ocean temperatures are in the right order of magnitude compared with the Phanerozoic proxy-derived trend[18]. The mean Phanerozoic tropical (25°S–25°N) sea-surface temperature is 29.67°C (standard deviation: 1.88°C) in series #1 (mean of 29.39°C and standard deviation of 0.45°C in series #2) compared to a mean of 28.1°C (standard deviation: 2.51°C) in the data compilation[18].

To generate the physical atmospheric boundary conditions required by cGENIE for each different continental configuration, we ran FOAM[51] general circulation model experiments for 2 to 3 kyrs, until deep-ocean temperature equilibrium. We then derived the 2D wind speed and wind stress, and 1D zonally-averaged albedo forcing fields required by the cGENIE model, using the 'muffingen' open-source software (DOI: 10.5281/zenodo.5500687), following the methods employed in ref[52]. Importantly, the FOAM

ocean-atmosphere simulations (and derived cGENIE forcing fields) account for topography on land, after ref.[24] (although topography is not shown in our maps for readability).

Simulations were initialized with a sea-ice free ocean and homogeneous temperature and salinity in the ocean (5 °C and 33.9 ‰, respectively) and integrated for a total of 20,000 years. Data is presented reflecting either the average over the last 5,000 years of the simulation (e.g., Fig. 2), or the mean and range of any oscillation over the last 5,000 years (e.g., Figs 1, 3), as detailed in the figure captions.

Principal component analysis

Principal components analyses (PCA) of Fig. 1 and Extended Data Fig. 5 were performed using, for each variable, the mean value simulated over the last 5000 years of the model simulations. For each variable, a total of 28 values was thus obtained (one value for each of the 28 time slices, from 540 Ma to 0 Ma every 20 Myrs). We considered 13 variables: surface $[O_2]$, subsurface $[O_2]$, benthic $[O_2]$, global $[O_2]$, global water age, benthic water age, sea-surface temperature ('SST'), benthic temperature, pCO_2, meridional overturning circulation maximum ('MOC max') and minimum ('MOC min'), export production ('export'; i.e., the flux of organic carbon produced in the ocean photic zone by primary producers that is not recycled (remineralised) before sinking deeper in the water column) and total ocean area. The PCA was conducted using the 'PCA' function of the R package 'FactoMineR'[53] and the first two axes / principal components were represented (capturing ca. 68 % of the variance in both cases). The objective here is not to provide a thorough PCA analysis but rather to (1) confirm the robustness of the correlations illustrated in the form of time-series and R^2 in the other panels of Fig. 1 and Extended Data Fig. 5 and (2) provide information on the correlation (or not) of additional key variables in a synthetic and graphical manner.

Additional discussion on ocean circulation regimes

Most of the simulations in Extended Data Figs. 8a and 8b show that ocean dynamics obtain

stable steady-state solutions. However, amongst these are cases where the system overshoots (for example, compare 0 Ma and 120 Ma in Extended Data Fig. 8a) before approaching a steady-state solution. This may imply the presence of an unstable oscillatory mode, in agreement with the linear stability analysis of low-resolution GCM steady states under present-day conditions[34,35]. The simulations in Extended Data Fig. 8 reveal that, depending on changes to continental configuration, the steady-state solutions can lose stability, resulting in stable oscillations. It is known that, under certain climate conditions, advective feedbacks in the ocean circulation can destabilize the steady state[54]. Simulations for 540 Ma and 500 Ma in Extended Data Figs.8a and 8b, respectively, are cases of steady-state solutions with oscillatory modes that are linearly stable, but only weakly stable, resulting in clear examples of damped oscillations. Since the frequencies of the damped and self-sustained oscillations (500 and 520 Ma in Extended Data Fig. 8b, respectively) are very similar, the transition could represent a Hopf bifurcation, resulting in self-sustained oscillations (characterized by fluctuations in circulation pattern and strength) around an unstable steady state.

In order to better understand the model behavior and ultimately, the nature of the state transitions in the global ocean circulation, we conducted additional cGENIE simulations using two contrasting, idealized continental configurations featuring either a latitudinal strip of land from the North Pole to the Southern Hemisphere mid latitudes ('Drake world'[55]), or a strip of land extending from the North Pole to the South Pole ('ridge world'[55]) (Extended Data Fig. 10). Drake world, with a pole free of land (i.e., purely oceanic at all longitudes), schematically represents the continental configuration of the early Paleozoic (or a high latitude circumpolar path such as in the late Cenozoic), while ridge world represents an early Mesozoic-like continental arrangement with landmasses present from the North Pole to the South Pole (see Fig. 2).

With Drake world, at low pCO_2 levels, deep-water formation takes place at the North

Pole, where a slightly higher hemispherical fraction of land cover with lower thermal inertia favors winter cooling over the surrounding ocean and thus convection (label #1 in Extended Data Figs. 10a and 10b). As atmospheric CO_2 is steadily increased across a series of experiments, the onset of a first set of oscillations, between ×5.5 and ×7.5 CO_2 (label #2), marks the appearance of a new mode of ocean circulation that stabilizes in the subsequent stable steady state at around ×8.25 CO_2 (label #3). Then, a new set of oscillations, from ×9 to ×9.75 CO_2, marks another step toward the weakening of the deep-water formation over the North Pole and strengthening over the South Pole (label #4). A third stable equilibrium finally stabilizes above ×10.75 CO_2 (label #5). Each set of oscillations thus marks the shift to a new regime of steady-state circulation and the ultimate result is a shift in the locus of deep-water formation from the North Pole (with lands barriers) to the South Pole (oceanic) in response to global warming from ×4 to ×16 CO_2. A comparable (but latitudinally reversed) behavior was previously observed by Pohl et al.[21] for the latest Ordovician. In response to global warming (their Figs. 4e to 4i, see also Extended Data Fig. 10c), the locus of deep-water formation shifts in their simulations from the South Pole (with lands) to the North Pole (oceanic). This is very similar to the change in ocean circulation simulated between 460 Ma and 440 Ma in simulation series #1 (Fig. 2), although the state transition here involves continental rearrangement in addition to global warming (global sea-surface temperature increases from 24.1°C at 460 Ma to 24.38°C at 440 Ma). No similar state transition is observed using the ridge world configuration (Extended Data Fig. 10a).

METHODS REFERENCES

47. Wilson, J. D., Monteiro, F. M., Schmidt, D. N., Ward, B. A. & Ridgwell, A. Linking Marine Plankton Ecosystems and Climate: A New Modeling Approach to the Warm Early Eocene Climate. *Paleoceanogr. Paleoclimatology* **33**, 1439–1452 (2018).

48. T. Reinhard, C. *et al.* Oceanic and atmospheric methane cycling in the cGENIE Earth system model - Release v0.9.14. *Geosci. Model Dev.* **13**, 5687–5706 (2020).
49. Velde, S. J. Van De, Hülse, D., Reinhard, C. T. & Ridgwell, A. Iron and sulfur cycling in the cGENIE. muffin Earth system model (v0.9.21). *Geosci. Model Dev.* **14**, 2713–2745 (2021).
50. Müller, R. D., Sdrolias, M., Gaina, C., Steinberger, B. & Heine, C. Long-term sea-level fluctuations driven by ocean basin dynamics. *Science* **319**, 1357–1362 (2008).
51. Jacob, R. L. Low frequency variability in a simulated atmosphere-ocean system. (University of Wisconsin Madison, 1997).
52. Crichton, K., Ridgwell, A., Lunt, D., Farnsworth, A. & Pearson, P. Data-constrained assessment of ocean circulation changes since the middle Miocene in an Earth system model. *Clim. Past Discuss.* 1–36 (2020) doi:10.5194/cp-2019-151.
53. Lê, S., Josse, J. & Husson, F. FactoMineR: An R package for multivariate analysis. *J. Stat. Softw.* **25**, 1–18 (2008).
54. Weijer, W. *et al.* Stability of the Atlantic Meridional Overturning Circulation: A Review and Synthesis. *J. Geophys. Res. Ocean.* **124**, 5336–5375 (2019).
55. Ferreira, D., Marshall, J. & Campin, J. M. Localization of deep water formation: Role of atmospheric moisture transport and geometrical constraints on ocean circulation. *J. Clim.* **23**, 1456–1476 (2010).
56. Garcia, H. *et al. World Ocean Atlas 2018, Volume 3: Dissolved Oxygen, Apparent Oxygen Utilization, and Dissolved Oxygen Saturation.* (2019).
57. Marsh, R. *et al.* Bistability of the thermohaline circulation identified through comprehensive 2-parameter sweeps of an efficient climate model. *Clim. Dyn.* **23**, 761–777 (2004).
58. DeVries, T. & Holzer, M. Radiocarbon and Helium Isotope Constraints on Deep

Ocean Ventilation and Mantle-3He Sources. *J. Geophys. Res. Ocean.* **124**, 3036–3057 (2019).

59. Song, H. *et al.* The onset of widespread marine red beds and the evolution of ferruginous oceans. *Nat. Commun.* **8**, (2017).

60. Melchin, M. J., Mitchell, C. E., Holmden, C. & Štorch, P. Environmental changes in the Late Ordovician-early Silurian: Review and new insights from black shales and nitrogen isotopes. *Geol. Soc. Am. Bull.* **125**, 1635–1670 (2013).

61. Pohl, A., Nardin, E., Vandenbroucke, T. R. A. & Donnadieu, Y. High dependence of Ordovician ocean surface circulation on atmospheric CO2 levels. *Palaeogeogr. Palaeoclimatol. Palaeoecol.* **458**, 39–51 (2016).

62. Meyer, K. M., Ridgwell, A. & Payne, J. L. The influence of the biological pump on ocean chemistry: implications for long-term trends in marine redox chemistry, the global carbon cycle, and marine animal ecosystems. *Geobiology* **14**, 207–219 (2016).

CODE AVAILABILITY

The version of the cGENIE code used in this paper is tagged as release v0.9.29 and has a DOI: 10.5281/zenodo.5885685. Necessary boundary condition files are included as part of the code release. Configuration files for the specific experiments presented in the paper can be found in the installation subdirectory: `genie-userconfigs/MS/pohletal.Nature.2022`. Details of the experiments, plus the command line needed to run each one, are given in the `readme.txt` file in that directory. A manual describing code installation, basic model configuration, and an extensive series of tutorials is provided (DOI: 10.5281/zenodo.5500696). The FOAM output is hosted on Zenodo (DOI: 10.5281/zenodo.5780096).

ACKNOWLEDGMENTS

The authors thank 4 anonymous reviewers for their comments, and J. Mossinger for editorial handling. This project has received funding from the European Union's Horizon 2020 research and innovation programme under the Marie Sklodowska-Curie grant agreement No. 838373. Calculations were partly performed using HPC resources from DNUM CCUB (Centre de Calcul de l'Université de Bourgogne). A.R. acknowledges support from NSF grants 1736771 and EAR-2121165, as well as from the Heising-Simons Foundation. This is a contribution to UNESCO project IGCP 735 "Rocks and the Rise of Ordovician Life" (Rocks n' ROL).

AUTHOR CONTRIBUTIONS

A.P. and A.R. designed the study and wrote the manuscript with input from all co-authors. AP. and A.R. conducted the FOAM and cGENIE experiments. A.P., A.R. and A.K. led the analysis of the model results. C.R.S. produced the continental reconstructions.

COMPETING INTERESTS

The authors declare no competing interests.

ADDITIONAL INFORMATION

Correspondence and requests for materials should be addressed to A.P. and A.R.

Peer review information.

Reprints and permissions information is available at www.nature.com/reprints.

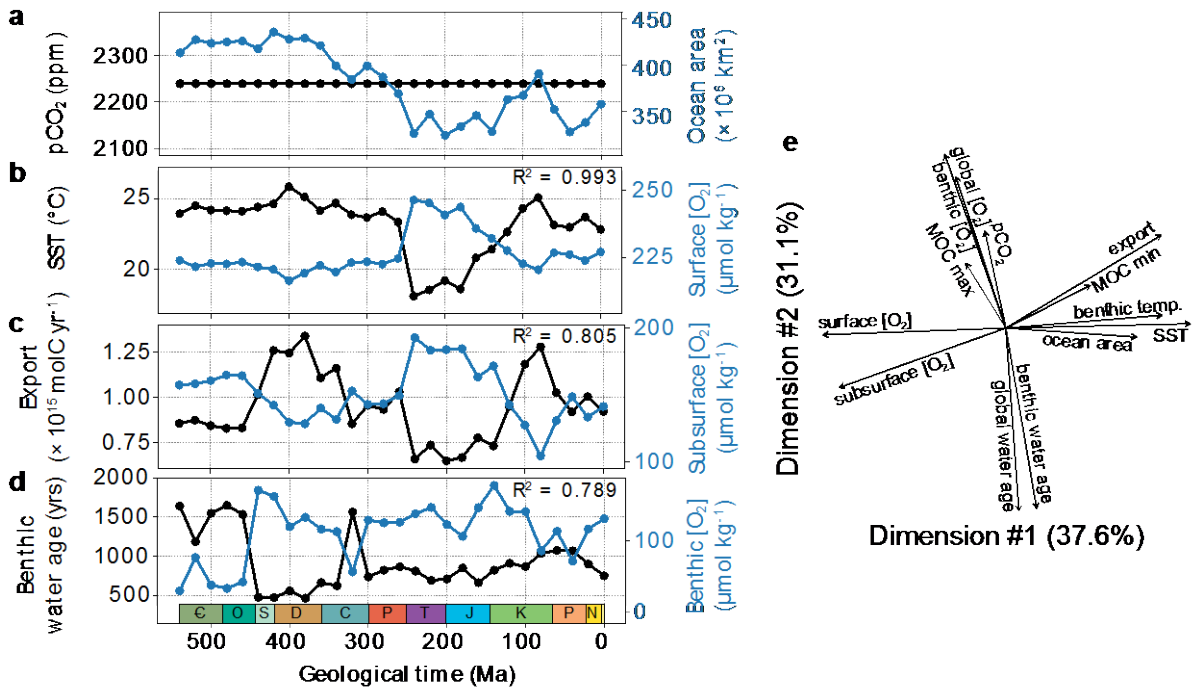
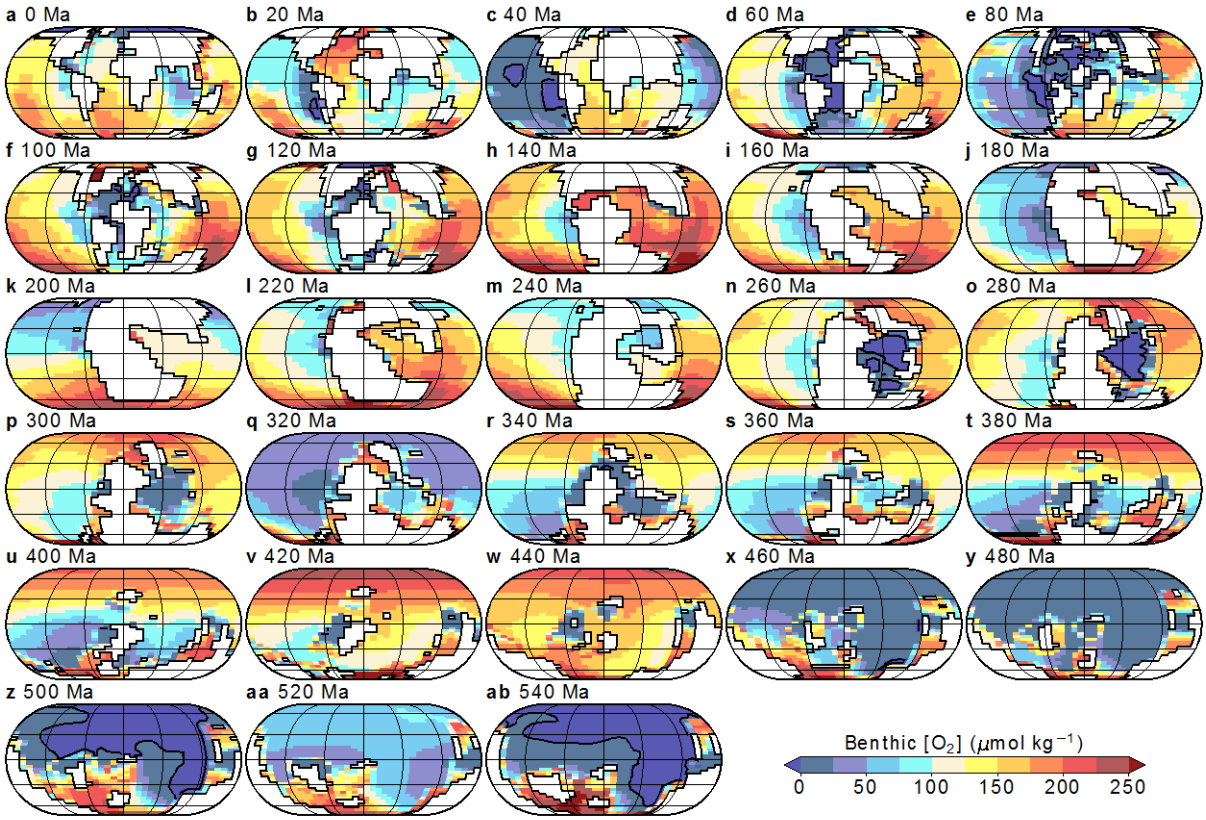


Figure 1. Earth System Model results for simulations at 2240 ppm CO_2 (series #1). (a) Atmospheric pCO_2 and global ocean area. (b) Globally averaged sea-surface temperatures and globally averaged ocean-surface oxygen concentrations. (c) Total export production and globally averaged subsurface (ca. 90–190 m depth) oxygen concentrations. (d) Globally averaged benthic water age and benthic oxygen concentrations, both extracted below 1000 m depth. For comparison, the present-day value is ~1050 years in the standard Modern cGENIE simulations of ref.[46]. (e) Principal component analysis (Methods). In panels b–d, the linear correlation coefficient (R^2) value is provided in the upper-right corner. For each variable and age, the mean value simulated over the last 5000 years of the model run is shown (point), while envelopes (grey shading) represent the range of values simulated over the same time interval (for simulations exhibiting oscillations). MOC: meridional overturning circulation.



538

539 Figure 2. Benthic oxygen concentrations for simulations at 2240 ppm CO_2 (series #1). Eckert
540 IV projection. Emerged continental masses are shaded white. Thick black line delimits the
541 extent of oceanic anoxia, defined as $[O_2] \leq 0$ μmol kg^{-1}. Results are averaged over the last
542 5000 years. See Extended Data Fig. 2 for magnified versions of 7 panels with redox proxy
543 data points and Extended Data Fig. 3 for the meridional overturning circulation and regions
544 of deep-water formation.

545

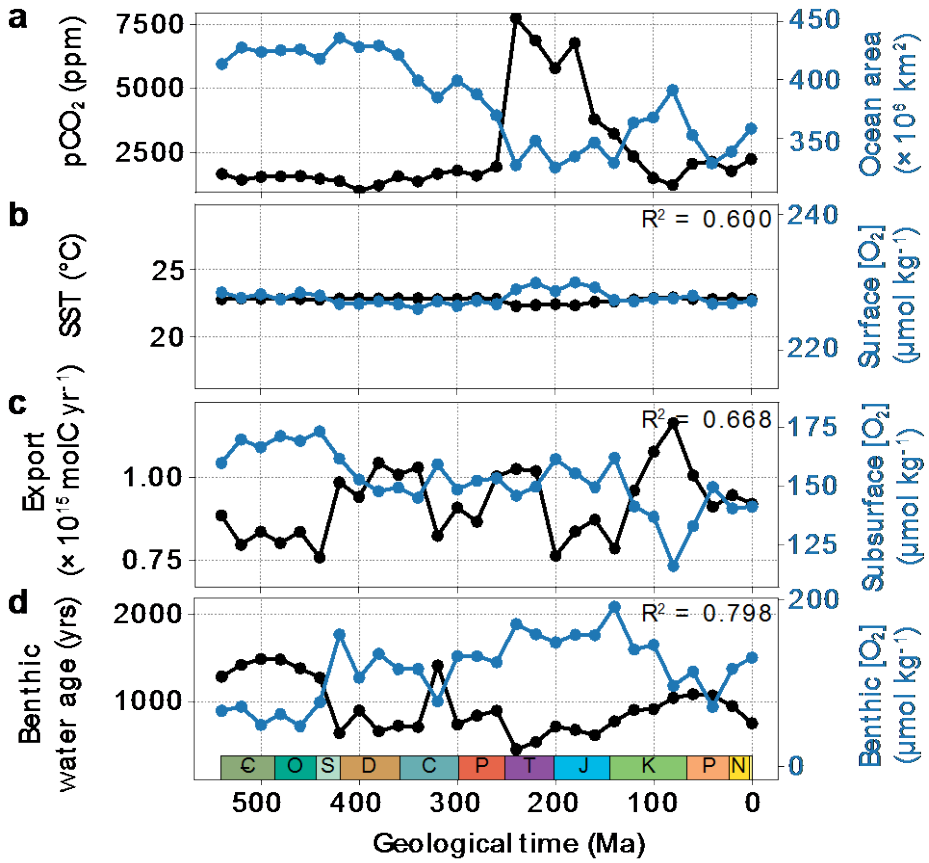
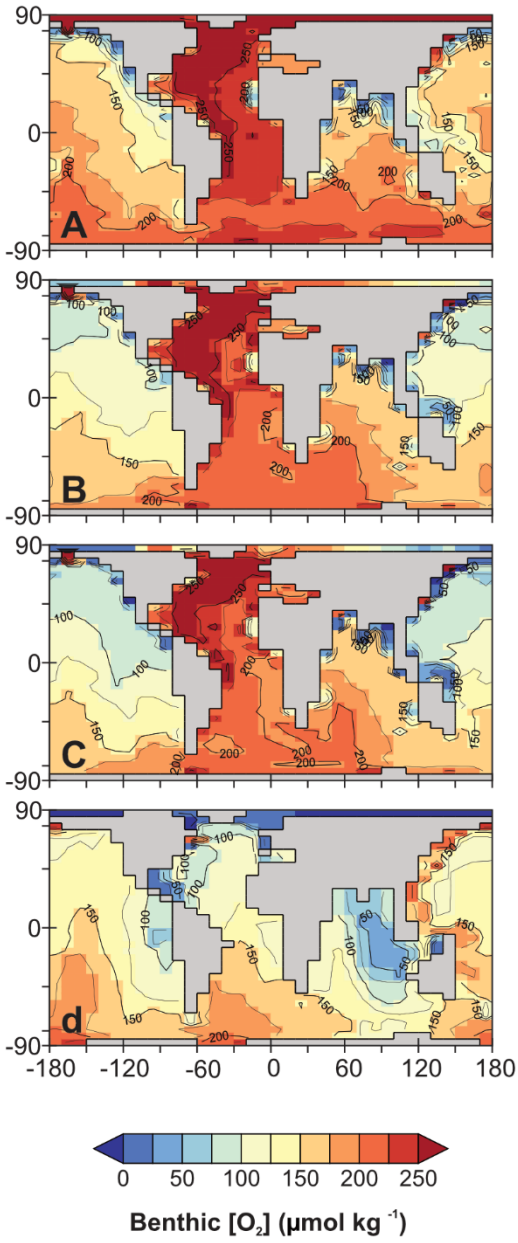


Figure 3. Panels (a-d) and panel description as per for Fig. 1, but for Earth System Model experiments in which we varied pCO_2 in order to approximately 'correct' for the paleogeographical impacts on climate (series #2), leaving surface oxygenation and mean global SST (b) largely invariant.

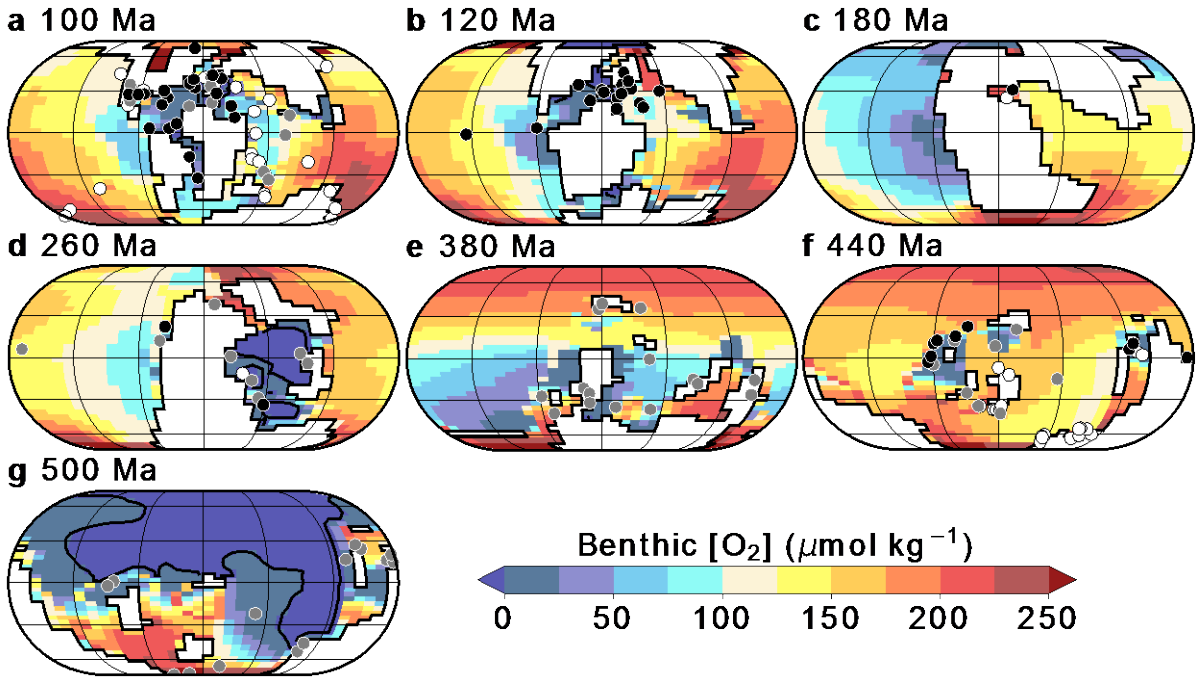


Extended Data Figure 1: Comparison of modern observations of seafloor dissolved oxygen ([O_2]) with the cGENIE model for different (modern) continental grids, boundary conditions, and biogeochemical cycling parameterization assumption. Projection is equal-area rectangular, and the color-scale is chosen to approximately match that in Figure 2. (a) Present-day distribution of [O_2] globally at the seafloor, for which we re-grid the World Ocean Atlas 2018[56] data to the modern continental grid of ref.[46] and show the oxygen concentration in the deepest model grid point. Apparent is both the production and southwards propagation (via North Atlantic Deep Water (NADW)) of highly oxygenated

563 waters from the North Atlantic, and oxygenated deep-water production and mixing around
564 Antarctica. (b) Benthic [O_2] distribution for the 'standard' modern ocean circulation of ref.[46]
565 run at 278 ppm CO_2, plus simplified biological export scheme. The large-scale patterns of
566 benthic [O_2] are reasonably reproduced, with the exception of too weak mixing of oxygen
567 around the Southern Ocean, itself caused by a weak simulated Antarctic Circumpolar Current
568 (ACC) and the difficulty in adequately representing the Drake Passage at this resolution. The
569 slightly too-low compared to observations values in the North Pacific are an additional
570 consequence of this. (c) Test of substituting the simplified biological export scheme of ref.[46]
571 with the explicit ecosystem model used here in the Phanerozoic series of simulations (but still
572 at 278 ppm CO_2). The slightly greater export simulated by the ecological model reduces
573 benthic [O_2] by ca. 10-20 μmol kg^{-1} while leaving the large-scale patterns largely unaltered.
574 (d) Deep-sea oxygenation in the 0 Ma Phanerozoic simulation (as per Figure 2, panel a) run
575 at 2240 ppm CO_2. Without flux adjustment applied in the simplified cGENIE 2D EMBM
576 atmosphere (see ref.[57]) there is virtually no NADW, explaining the relatively poor and South-
577 to-North oxygenation of the Atlantic. The Indian Ocean is also too poorly oxygenated,
578 although the general pattern in the Pacific is reproduced. There are several main reasons for
579 this model-data mismatch. Firstly, directly re-gridding from a relatively coarse resolution
580 GCM (FOAM) creates a highly restricted and shallow Drake Passage (Extended Data Figure
581 7a, 0 Ma), precluding a strong ACC forming. More pertinently, the Phanerozoic simulation
582 series (Figure 2) are all run at 2240 ppm. The resulting much-warmer-than-modern ocean is
583 associated with the absence of any sea-ice formation and lower seawater oxygen solubility,
584 likely explaining at least some of the spatial pattern and much of the lower global mean [O_2]
585 inventory (Extended Data Figure 8a, 0 Ma). In terms of ventilation and water mass idealized
586 mean age (not shown), the Atlantic, lacking an AMOC is far too old, whereas the Indian and

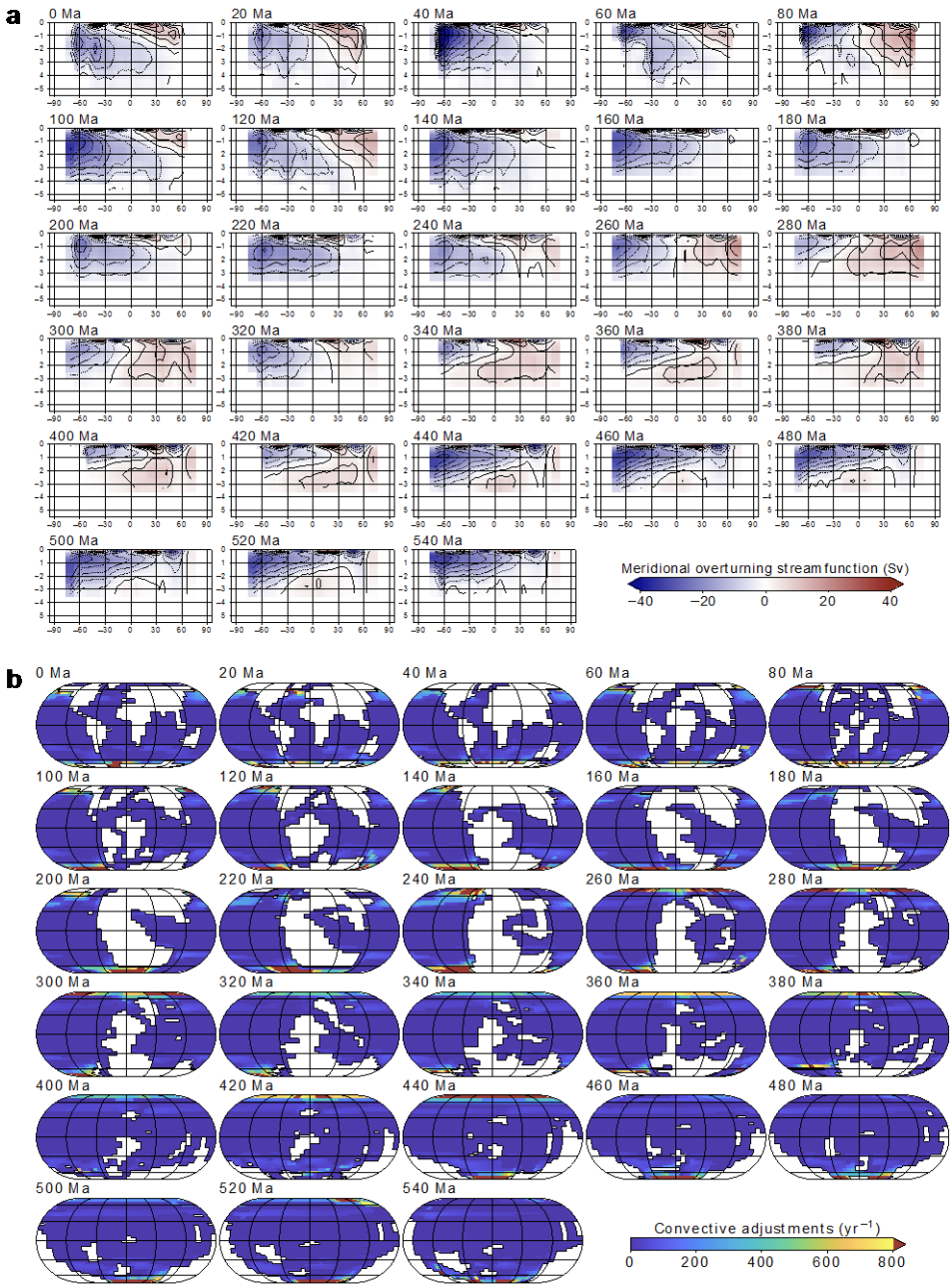
587 Pacific oceans are similar to the inverse modelling of ref.[58] despite the aforementioned issues

588 with the Drake Passage and that the 0 Ma simulation is run at 2240 ppm CO_2.



Extended Data Figure 2: Selected redox proxy data vs. the corresponding model oxygenation realization. Benthic oxygen concentrations for simulations at 2240 ppm CO_2 (series #1). Eckert IV projection. Emerged continental masses are shaded white. Thick black line delimits the extent of oceanic anoxia, defined as $[O_2] \leq 0$ µmol kg^{-1}. Results are averaged over the last 5000 years. Black (white) dots represent anoxic (oxic) conditions and grey points represent possible or intermittent anoxia, for 100 Ma after ref.[28], for 120 Ma after ref.[27], for 180 Ma after ref.[30], for 260 Ma after ref.[26], for 380 and 500 Ma after ref.[59], and for 440 Ma after ref.[60]. These time slices have been chosen to represent regularly-spaced periods during the Phanerozoic, typified by oceanic anoxic events. The last 100 Myrs are deliberately left aside because (i) the ocean is overall well oxygenated during this time interval and (ii) our constant boundary conditions (deliberately chosen to isolate the role of tectonics from climate, see main text) do not (and indeed, do not intent to) reproduce the pronounced cooling trend through the Cenozoic (especially from Early Eocene Climate Optimum (ca. 50 Ma) onwards), precluding direct model-data comparison.

606



607

608 Extended Data Figure 3: Deep-ocean circulation for simulations at 2240 ppm CO_2 (series #1).

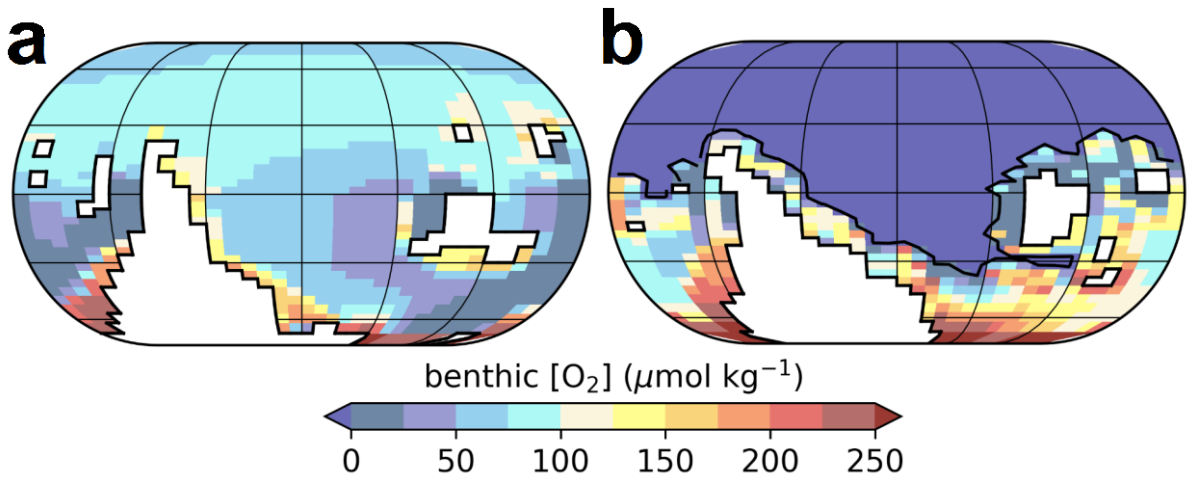
609 (a) Meridional overturning stream function, in Sv (sverdrup, 1 Sv = 10^6 m^3 s^{-1}). A negative

610 (blue) stream function corresponds to an anticlockwise circulation. (b) Annual distribution of

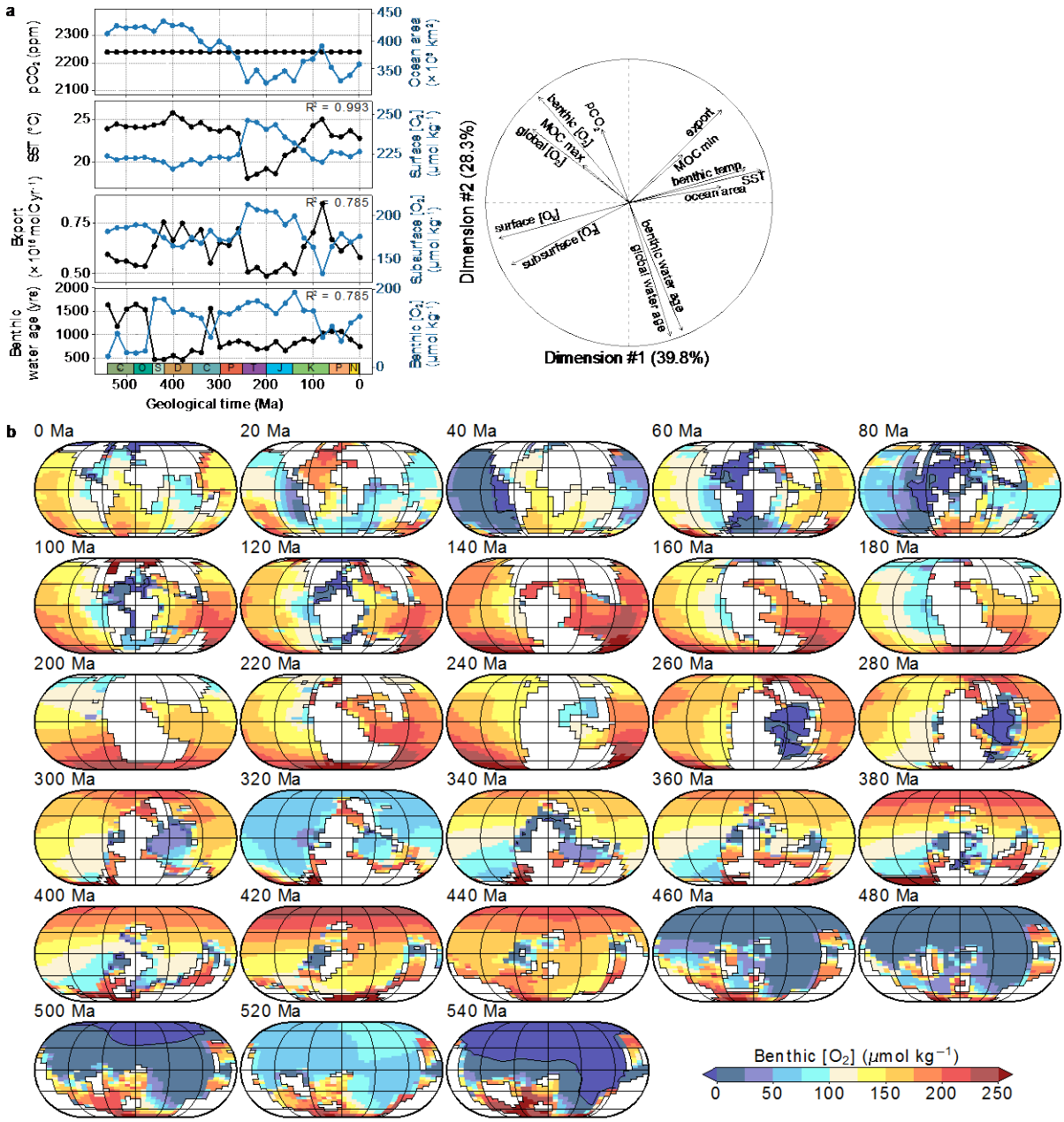
611 convective adjustments across the water column. Emerged continental masses are shaded

612 white. Eckert IV projection. Results are averaged over the last 5000 years.

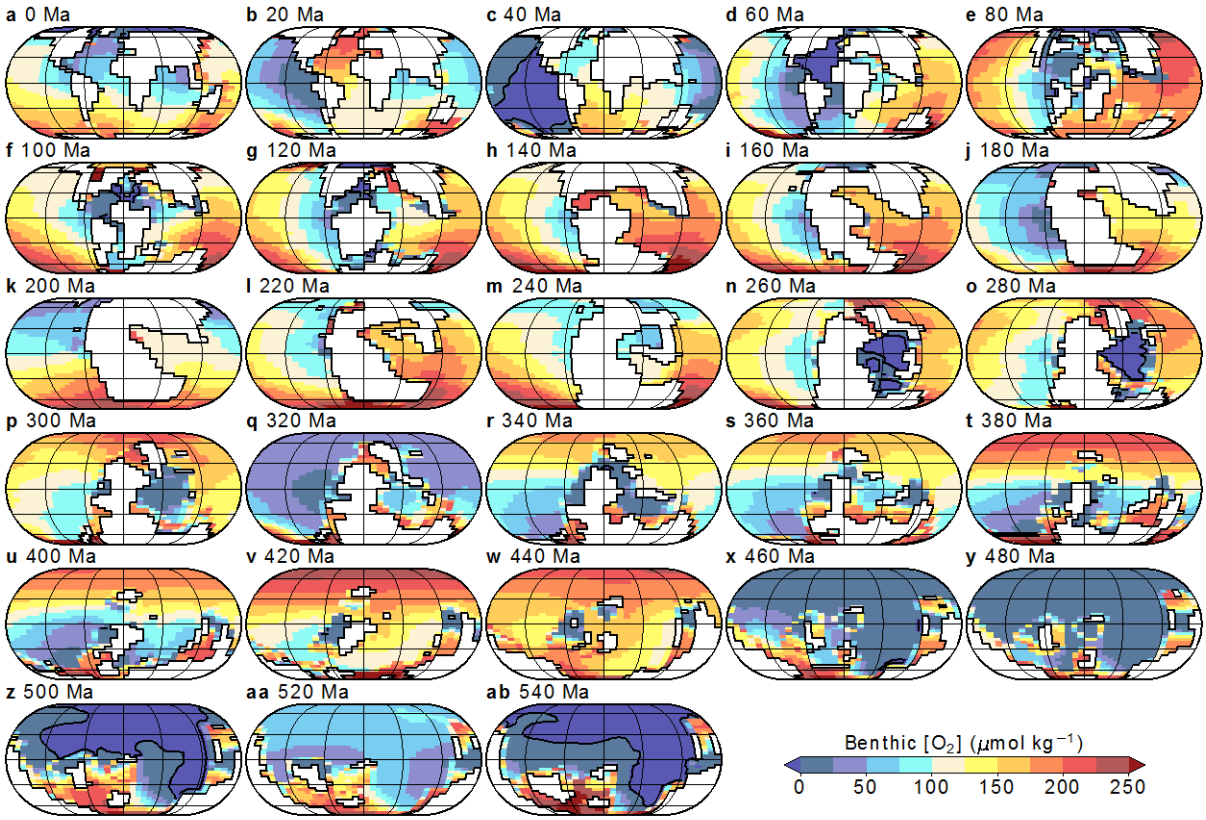
613



Extended Data Figure 4: Benthic oxygen concentrations for simulations at 2240 ppm CO_2 (like series #1) at 440 Ma (a) and 460 Ma (b), using the continental reconstructions of BugPlates[31], with topography/bathymetry after ref.[61]. Eckert IV projection. Emerged continental masses are shaded white. Thick black line delimits the extent of oceanic anoxia, defined as $[O_2] \leq 0$ μmol kg^{-1}. Results are averaged over the last 5000 years. Panels (a) and (b) are identical to panels (w) and (x) of Fig. 2 except that simulations have been conducted using another continental reconstruction. Note that although we simulate sulphate reduction in cGENIE, with SO_4^{2-} being used as the electron acceptor for the remineralization of organic matter in the ocean interior once dissolved O_2 has become depleted (see ref.[48]), small negative O_2 concentrations can arise when multiple geochemical reactions compete simultaneously for the same depleted oxygen pool. However, because the product of sulphate reduction – hydrogen sulphide (H_2S) – has fast oxidation kinetics in the presence of free oxygen, the transport of H_2S from anoxic to oxic areas closely mirrors the transport and fate of 'negative oxygen' (see ref.[62]) and the overall redox landscape is largely independent of this small modelled oxygen over-consumption.



Extended Data Fig. 5. Earth System Model results for simulations at 2240 ppm CO_2 (like #1) but with no dependence of remineralization on temperature. (a) Same as Fig. 1. (b) Same as Fig. 2.



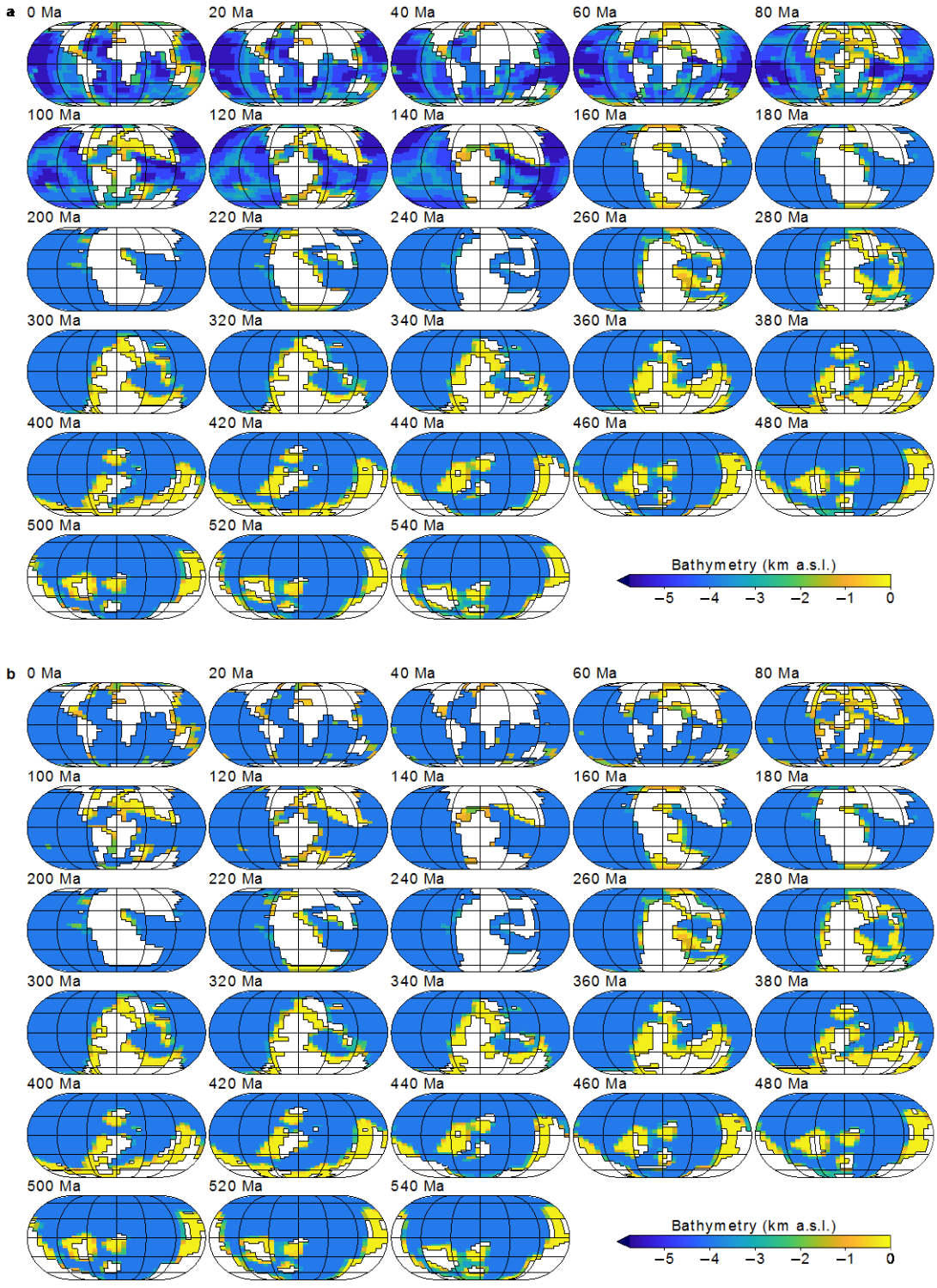
639

640 Extended Data Figure 6. Benthic oxygen concentrations for simulations at 2240 ppm CO_2

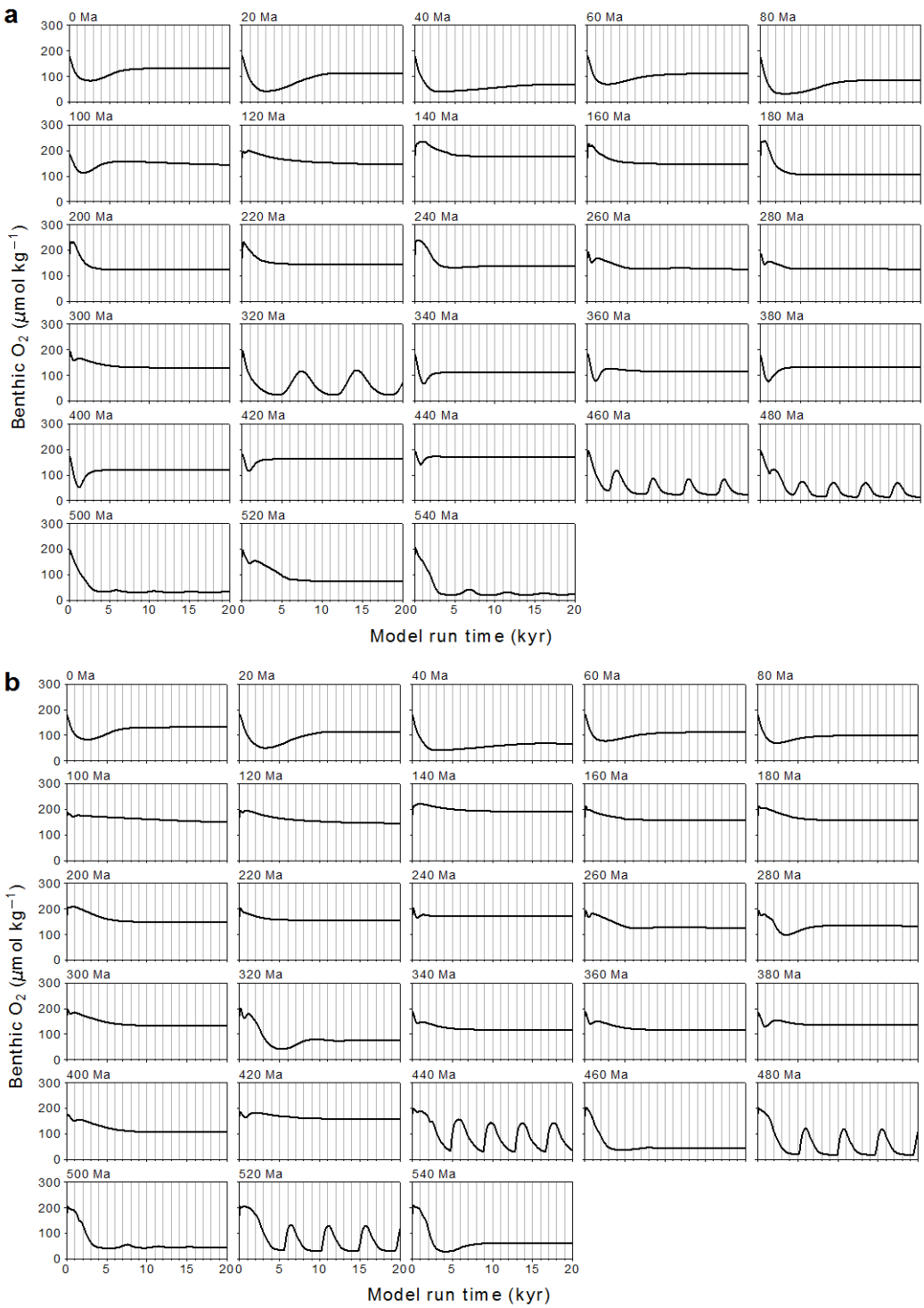
641 (like #1) but with no mid-ocean ridges (see Extended Data Fig. 7). Results are averaged over

642 the last 5000 years. Emerged continental masses are shaded white. Eckert IV projection.

643



Extended Data Fig. 7: Bathymetry with mid-ocean ridges used in series #1 and #2 (a), and flat-bottomed bathymetric reconstructions used in simulations with no mid-ocean ridges (b) (see Extended Data Fig. 6). Only reconstructions for 0 to 140 Ma (both included) differ (see Methods). Emerged continental masses are shaded white. Eckert IV projection.



649

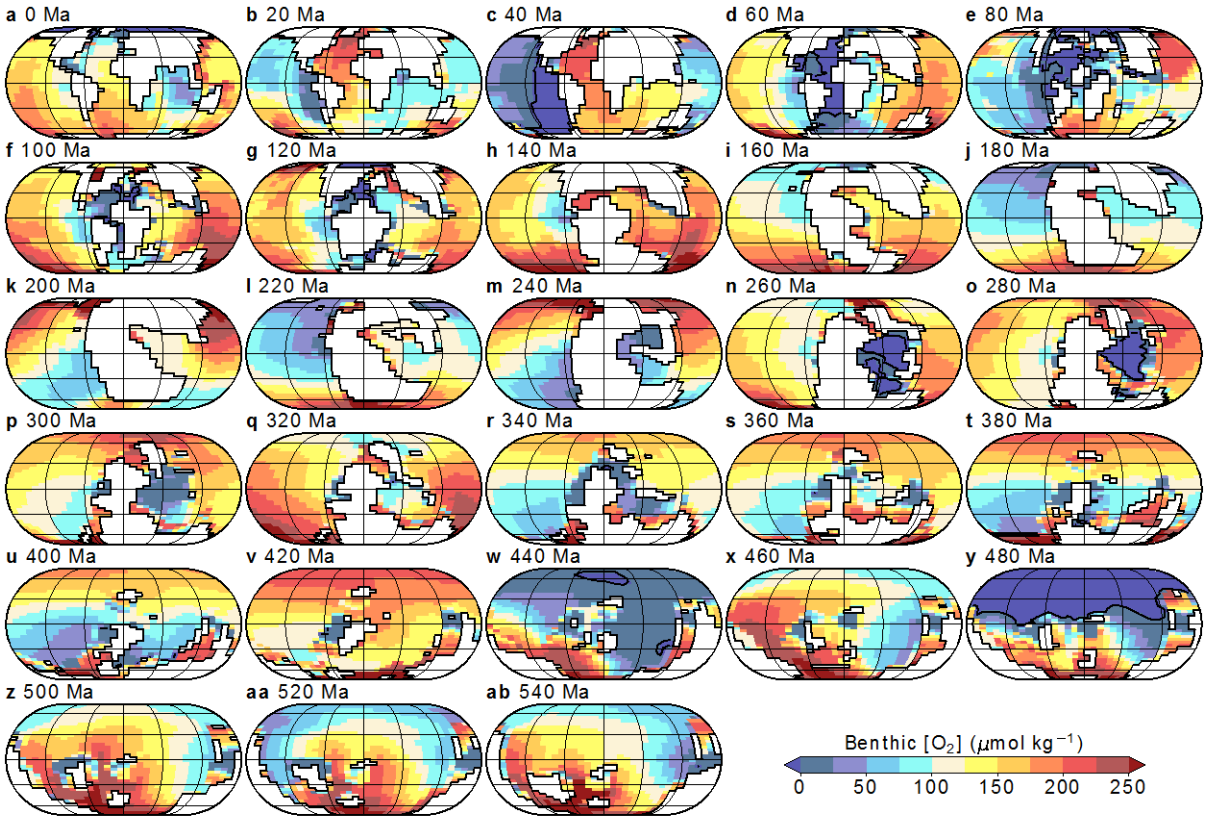
650 Extended Data Figure 8. Time-evolution of benthic [O_2]. (a) Simulations at 2240 ppm CO_2

651 with temperature-dependent remineralization (series #1). (b) Simulations in which we varied

652 pCO_2 in order to approximately 'correct' for the paleogeographical impacts on climate (series

653 #2).

654



655

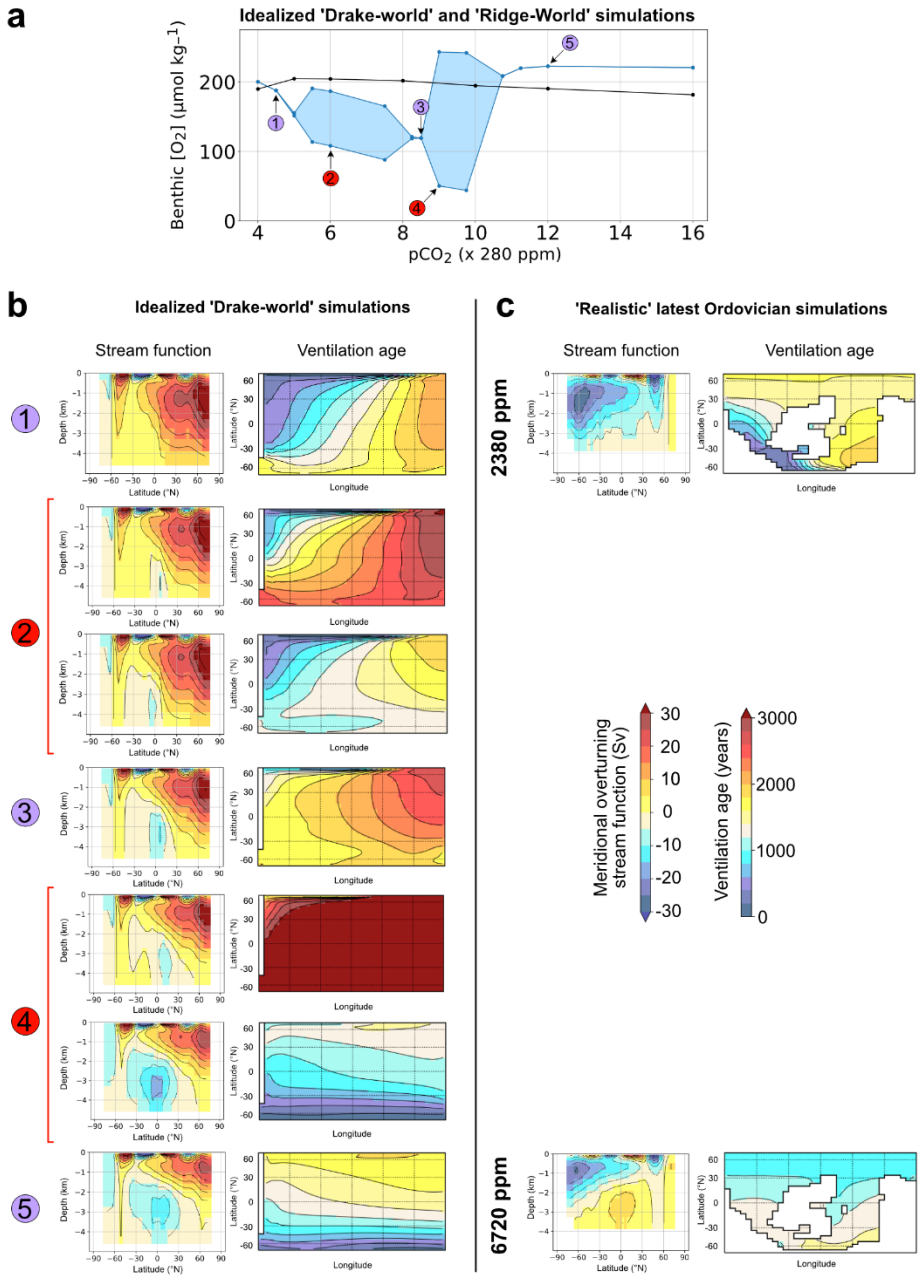
656 Extended Data Figure 9. Benthic oxygen concentrations for simulations at 1120 ppm CO_2,

657 with temperature-dependent remineralization and mid-ocean ridges. Emerged continental

658 masses are shaded white. Results are averaged over the last 5000 years. Eckert IV projection.

659

660



Extended Data Figure 10: Ocean circulation regimes in the cGENIE model. (a) Envelope of benthic [O_2] values simulated at various atmospheric CO_2 levels using Drake world (in blue, see maps in panel (b)) and ridge world (in black) (Methods). Regimes of stable equilibria and regimes of stable oscillations for Drake World simulations are numbered and labelled using a blue and red background, respectively. (b) Meridional overturning stream function in Sv (sverdrup, 1 Sv = 10^6 m^3 s^{-1}) and map of benthic ventilation age for each stable equilibrium and the 2 extreme states of each stable oscillatory regime identified in panel (a), using same

numbering and color code. Lambert cylindrical equal-area projection. A negative (blue) stream function corresponds to an anticlockwise circulation. (c) Tentative comparison with the latest Ordovician simulations of Pohl et al.[21]. Results are shown at 6720 ppm and 2380 ppm CO_2, corresponding to the warm and cold states of Scenario #1 in ref.[21].